ACS APPLIED MATERIALS & INTERFACES

Research Article

www.acsami.org

Hierarchical Structure and Mechanical Improvement of an n-HA/GCO–PU Composite Scaffold for Bone Regeneration

Limei Li, Yi Zuo,* Qin Zou,* Boyuan Yang, Lili Lin, Jidong Li, and Yubao Li*

Research Center for Nano-Biomaterials, Analytical & Testing Center, Sichuan University, Chengdu 610064, People's Republic of China

ABSTRACT: To improve the mechanical properties of bone tissue and achieve the desired bone tissue regeneration for orthopedic surgery, newly designed hydroxyapatite/polyurethane (HA/PU) porous scaffolds were developed via in situ polymerization. The results showed that the molecular modification of PU soft segments by glyceride of castor oil (GCO) can increase the scaffold compressive strength by 48% and the elastic modulus by 96%. When nano-HA (n-HA) particles were incorporated into the GCO–PU matrix, the compressive strength and elastic modulus further increased by 49 and 74%, from 2.91 to 4.34 MPa and from 95 to 165.36 MPa, respectively. The n-HA particles with fine dispersity not only improved the interface bonding with the GCO–PU matrix but also provided effective bioactivity for bonding with bone tissue. The hierarchical structure and mechanical quality of the n-HA/GCO–PU composite scaffold were determined to be appropriate for the growth of cells and the regeneration of bony tissues, demonstrating promising prospects for bone repair and regeneration.

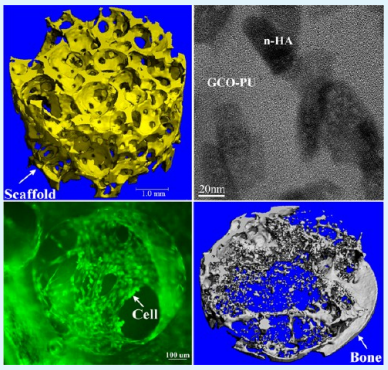

KEYWORDS: *nanohydroxyapatite, polyurethane composite, hierarchical structure, mechanical quality, bone regeneration*

1. INTRODUCTION

The conflict between increasing patient demand and limited clinical substitutes has stimulated numerous researchers to explore multifunctional biomaterials and improve the synthesis efficiency of conventional methods.[1] Materials that have been copied from nature to build synthetic structural composites are referred to as architectural configuration. Rigid biological materials, such as bone and sponge spicules, are attractive for their unusual combination of components with unique properties.[2]

After the bone mineral phase, nanohydroxyapatite crystals primarily intercalate into the collagen matrix due to complex bonding; the resulting hard bony tissue combines strength and ductility to enable high-energy absorption prior to failure.[3] This combination presents a hierarchical structure from the microscale to the nanoscale. Thus, bone tissue, which is a natural structural composite, has evolved to fulfill a variety of functions.[4]

Matching structure to function is a challenge for synthetic biomaterials. The distribution of nanohydroxyapatite crystals in an organic matrix enables a composite to achieve superior mechanical properties and bone-bonding bioactivity. A porous structure for bone ingrowth should mimic the diameter of osteon (190–230 μm) or cancellous bone (500–600 μm) over a minimum pore size of 100 μm.[5] Substantial effort has focused on building composites with a hierarchical structure and desirable mechanical qualities and tissue regeneration capacity.[6−8]

Recently, the combination of nanohydroxyapatite (n-HA) particles and polyurethane (PU) block copolymer has provided the opportunity to establish a hierarchical structure and realize biological function. PU is an elastomer with adjustable mechanical properties endowed by its soft and hard segments,[9,10] especially simultaneous foaming, which occurs during its in situ polymerization. Using a bottom-up approach, a porous n-HA/PU composite with a hierarchical structure and improved characteristics can be fabricated. The composite scaffold can be structured in three levels: the hard/soft block structure at the molecular level, the hydroxyapatite particles dispersed in a PU matrix at the nanolevel, and the porous structure at the microlevel. The three-level structures resemble segmented collagen, the mineral in an organic matrix and the cancellous structure of natural bone, which comprise the material basis of a high-performance scaffold for bone regeneration.

Porous PU/HA and PU/bioglass composites have demonstrated the ability to support cell proliferation[11] or tissue regeneration,[12−14] in which different pore-forming methods, including salt leaching, sponge impregnation and fiber electrospinning, have been reported. However, the mechanical properties of PU-based composite scaffolds remain too weak to match those of cancellous bone (mechanical strength >2 MPa, Young's modulus >0.05 GPa)[5] and provide adequate supporting strength. The PU/bioglass porous composite has a strength of 0.10 MPa and a modulus of 1.35 MPa, which are at least 1 order of magnitude weaker than the strength and modulus of natural cancellous bone.[14] When the HA component or agglomerated n-HA powder was blended, a

Received: August 8, 2015
Accepted: September 25, 2015
Published: September 25, 2015

DOI: 10.1021/acsami.5b07327
ACS Appl. Mater. Interfaces 2015, 7, 22618–22629

Young's modulus of 1.26 MPa[13] or 0.32 MPa[15] for the PU/HA scaffolds and a mechanical strength of 0.11 MPa was attained.[16] Significant improvement in the mechanical properties by careful optimizations is important.[14]

Due to an extremely large specific surface, n-HA crystals tend to naturally agglomerate after drying or blending in polymer matrix,[13,17] which differs from the nanoscale fine dispersion of bone apatites in natural bone. From the viewpoint of fracture-mechanics, the nanometer apatite crystals of natural bone play a key role in enabling the bone tissue to achieve superior mechanical properties.[18] Although polymerization and the biological performance of PU-based composites have been preliminary investigated,[19,20] few studies have addressed the structure−property relation.[21] The effect of PU matrix modification and the substitution of nano-HA particles for micro-HA particles on the mechanical properties of HA/PU composites requires additional investigation. The role of an organic PU matrix or the inorganic filler in the mechanical performance remains a controversial topic.[3,22]

To investigate the impact of segment modification and inorganic filler on the mechanical properties of PU scaffolds, pristine castor oil (CO) and alcoholized castor oil (i.e., glyceride of castor oil, GCO) were separately employed to construct PU scaffolds (named CO−PU and GCO−PU, respectively) according to our assumption that the alcoholization of castor oil may effectively provide more OH groups for pristine castor oil, which increases the mechanical properties of a PU matrix. Nano-HA particles were utilized to prepare composite scaffolds (named n-HA/CO−PU and n-HA/GCO−PU) to investigate their influence on the mechanical performance of a PU matrix. The μ-HA/PU composite scaffolds were also fabricated to verify the positive effect of n-HA particles on the mechanical properties. The physicochemical properties were analyzed by Fourier transform infrared spectroscopy (FTIR), X-ray diffraction (XRD), X-ray photoelectron spectrometry (XPS), nuclear magnetic resonance (NMR), dynamic mechanical analysis (DMA), scanning electron microscopy (SEM), transmission electron microscopy (TEM), mechanical tests, and micro computed tomography (micro-CT) analyses. The cell behavior and bone regeneration capacity of the selected composite scaffold were also evaluated via in vitro rat bone marrow stem cells (MSCs) culture and in vivo implantation in a rabbit femoral condyle. A scaffold with a hierarchical structure, good mechanical qualities and effective bone regeneration capacity can be a suitable candidate for bone repair and regeneration.

2. EXPERIMENTAL SECTION

2.1. Scaffold Fabrication. *2.1.1. Reagents.* Pharmaceutical grade castor oil, AR-grade glycerin, and isophorone diisocyanate were purchased from Shanghai Aladdin Co. Ltd., China. All other chemicals of AR grade were purchased from the Chengdu Kelong Co. Ltd., China.

2.1.2. Synthesis of Nanohydroxyapatite. The n-HA particles were prepared according to the wet chemical method without later sintering or heat treatment. A 0.3 M aqueous solution of $Na_3PO_4{\cdot}12H_2O$ was added dropwise into a 0.5 M aqueous solution of $Ca(NO_3)_2{\cdot}4H_2O$ at 70 °C under stirring for 1 h. The pH was adjusted to 10 with NaOH solution, and polyethylene glycol (PEG400) was employed as a surface dispersant. After reaction, the n-HA precipitate was aged for 24 h at room temperature. The slurry was freeze-dried at −50 °C for 1 week. Micrometer-sized hydroxyapatite (μ-HA) powder with a particle diameter range of approximately 5−15 μm was also fabricated by spray drying from the n-HA slurry.[23]

2.1.3. Alcoholization of Castor Oil. The alcoholization of castor oil was performed in a round-bottom flask equipped with heating and a mechanical stirrer.[24] A total of 2.5 mol of glycerin was mixed with 1.0 mol of castor oil (CO), and 0.05 wt % CaO as a catalyst in relation to the total mass of the reagents was added to the vessel. The reaction was performed in a nitrogen atmosphere at 200 °C for 1 h. The unreacted glycerin in the bottom was separated after stopping the conversion by adding phosphoric acid. After alcoholization, the hydroxyl value increases from 159 of pristine castor oil to 288 of GCO, as tested according to the Chinese industry standard (SN/T 0801.20−1999).

2.1.4. Fabrication of HA/PU Composite Scaffolds. The HA/PU composite scaffolds with 40 wt % HA were fabricated by in situ polymerization and simultaneous foaming.[16] First, 30 g of CO or GCO was mixed with 40 g of μ-HA powder or n-HA particles in a 250 mL three-necked flask under nitrogen atmosphere and thorough stirring. Then, 30 g of isophorone diisocyanate (IPDI) was added to the mixture, and the reaction was maintained at 70 °C for 3 h to obtain the prepolymer. Subsequently, 1 mL of 1,4-butanediol was employed as a chain extender to extend the prepolymer and 0.2 mL of deionized water was added to the cross-linked prepolymer under stirring for 30 min. The resultant mixture was cured at 110 °C accompanied by simultaneous foaming. In this procedure, six types of scaffolds were obtained: CO−PU, GCO−PU, n-HA/CO−PU, n-HA/GCO−PU, μ-HA/CO−PU and μ-HA/GCO−PU, in which CO−PU indicates that the PU was made from castor oil and GCO−PU indicates that the PU was made from glyceride of castor oil.

2.2. Physical, Mechanical, and Chemical Characterization of Scaffolds. *2.2.1. XRD Analysis.* The X-ray diffraction (XRD) patterns of the composites were obtained by XRD (DX2500, China) with Cu Kα radiation at 40 kV and 25 mA. Scans were in the 2θ range from 10 to 70° with a step size of 0.03°.

2.2.2. FTIR Analysis. The Fourier transform infrared (FTIR) spectra were recorded in the transmission mode from wavenumber 4000 to wavenumber 400 cm^{-1} (Nicolet 6700). The representative spectra of the PU component in the wavenumber region from 1200−2000 cm^{-1} were selected for presenting the characteristic PU phase.

2.2.3. Mechanical Test. The compressive strength and modulus of the composite scaffolds were determined using a mechanical testing machine (AUTOGRAPH AG-IC 20/50KN, Japan). According to the ASTM D 5024-95 standard, the HA/PU scaffolds were cut into a specimen size of 10 × 10 × 20 mm^3. The cross-head speed was set to 0.5 mm/min, and the load was applied until the specimen was compressed to approximately 40% of its original length. The experiment was performed in quintuplicate.

2.2.4. Porosity Measurement. The porosity of the scaffold was measured by liquid displacement as an average value of five samples, which is similar to the reported method.[25] In this method, water (density, ρ) was employed as the displacement liquid. A dry sample with weight W_1 and volume V was immersed in a cylindrical vessel that contained water. The sample was kept in the water, and a series of evacuation-repressurization cycles were conducted to force the water into the pores of the scaffold. Cycling was continued until no air bubbles emerged from the scaffold. The total weight of the water-impregnated scaffold was recorded as W_2.

The porosity (P) of the scaffold was calculated by

$$P\ (\%) = \frac{W_2 - W_1}{\rho V} \times 100$$

2.2.5. XPS Analysis. The binding energies of the PU composites were acquired by X-ray photoelectron spectroscopy (XPS, AXIS Ultra DLD, UK). The data analysis was performed with the XPS Peak Fit 4.1 software. The molar concentration ratios were calculated from the peak areas (linear background subtraction), which were normalized based on the acquisition parameters. The N 1s peaks were decomposed with a Lorentzian−Gaussian (20% of Lorentzian) product function and the full width of half-maximum (fwhm) for all N 1s peaks was constrained to 1.4 eV.

2.2.6. NMR Analysis. The chemical composition of the composites was analyzed by ^{13}C solid nuclear magnetic resonance (^{13}C NMR,

DOI: 10.1021/acsami.5b07327
ACS Appl. Mater. Interfaces 2015, 7, 22618−22629

Scheme 1. Chemical Structures of (A) CO−PU and (B) GCO−PU, Which Show a Greater Intermolecular Hydrogen Bond (Red Cuboid) Due to More OH Groups and Small Steric Hindrance of GCO, and Chemical Reactions of (C) Allophanate and (D) Biuret

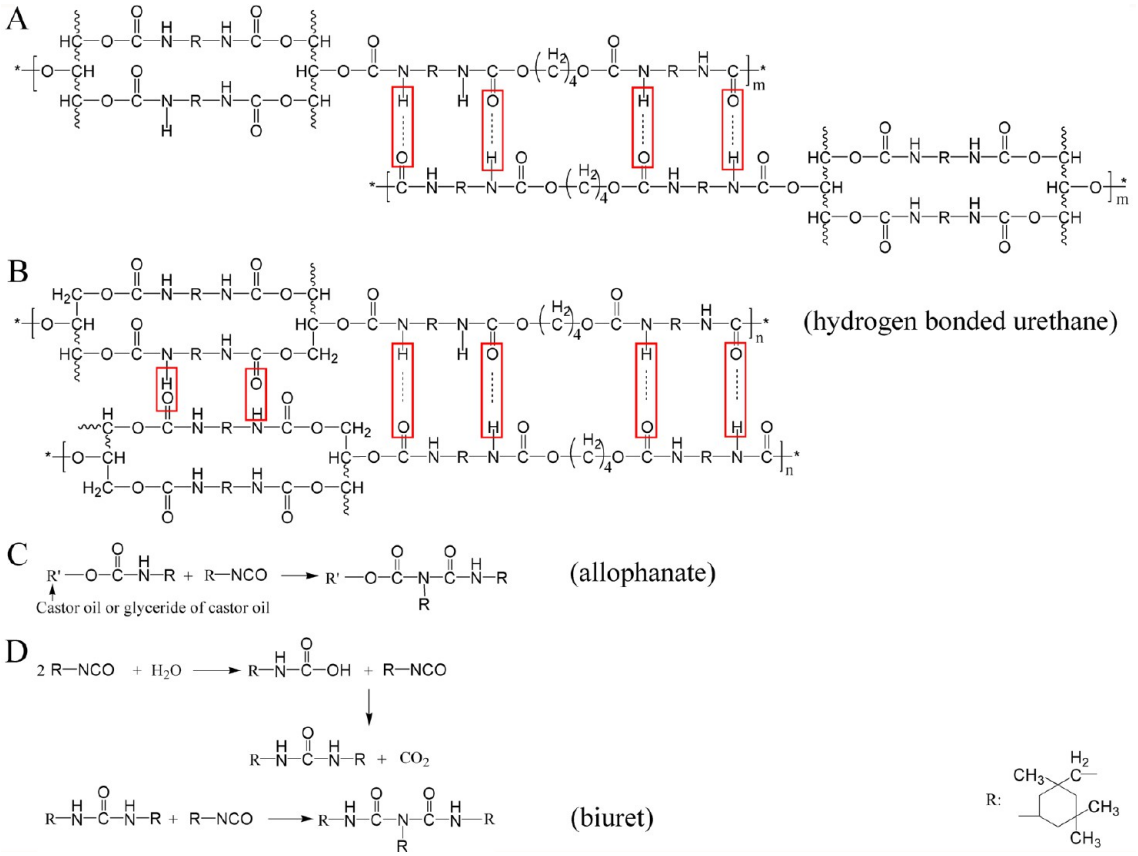

Bruker, Switzerland) using a 500 MHz spectrometer for ^{13}C nuclei at room temperature.

2.2.7. DMA Analysis. The PU composites were tested on a dynamic mechanic analyzer (NETZS CH DMA 242, Germany) using a large compression module with an applied force (F) that ranged from 1 to 5 N at 1 Hz by a temperature ramp from −100 to 150 °C.

2.2.8. SEM and TEM Observation. The composite microstructure was observed by scanning electron microscopy (SEM, JSM-6500LV, Japan). The morphology of the μ-HA particles and n-HA particles and the labeled image of the PU hard segment were observed by transmission electronic microscopy (TEM, Tecnai, G2 F20). A cryogenic ultramicrotome was employed to make ultrathin composite samples. Ruthenium tetroxide (RuO_4)[26] was employed as a staining agent of the PU hard segment, with an exposure time of 15 min.

2.2.9. 3D Imaging. A computed microtomographic system (μCT40 scanner, Scanco Medical, Switzerland) was employed to scan the scaffold block with a volume of 106 mm^3. The instrument was operated at 45 kV and 175 μA, and a total of 198 microtomographic slices with a slice increment of 19 μm were extracted for each sample. The 3D reconstructed image of the scaffold was acquired from a series of 212 serial 2048 × 2048 bitmap images.

2.3. Cytocompatibility In Vitro. *2.3.1. Cell Culture and Seeding.* SD rats with a weight of approximately 100 g were employed as donors of femurs and tibiae for bone marrow harvesting and primary MSCs isolation according to the established procedure. MSCs at the third passage were utilized in the experiments. The n-HA/GCO−PU scaffold was cut into square samples (10 × 10 × 2 mm). After ultrasonic rinsing in distilled water and autoclave sterilization, the samples were cocultured with MSCs (2×10^4 cells/well) in 24-well plates compared with the blank control (tissue culture plastic), which was equilibrated in α-MEM medium (Gibco, 1 mL/well) in a humidified incubator (37 °C, 5% CO_2).

2.3.2. Cell Morphology. The morphology and spreading of the MSCs growing on the scaffold samples were observed with SEM (JSM-6510LV, JEOL, Japan) and fluorescence microscopy (TE 2000-U, Nikon Eclipse, Japan). Prior to the SEM observation, the samples were rinsed with PBS, fixed with 2.5 vol % glutaraldehyde, dehydrated through graded ethanol, and dried by CO_2 critical point. For the fluorescence observation, the cells were labeled with the live/dead reagent (LIVE/DEAD Viability/Cytotoxicity Kit, Life Technologies).

2.3.3. Cell Proliferation. The proliferation of the MSCs that were cultured with the scaffold samples for 1, 4, 7, and 11 day(s) was evaluated with an MTT (3-[4,5-dimethylthiazol-2-yl]- 2,5-diphenyl-2*H*-tetrazolium bromide, Amresco) assay with a multilabel counter (Wallac Victor3 1420, PerkinElmer Co.) at 490 nm.

2.3.4. Cell Differentiation. The osteocalcin (OCN) content in the culture medium was measured at 1, 4, 7, and 11 day(s) using the rat bone Gla protein/osteocalcin (BGP/OCN) ELISA kit according to the manufacturer's protocol. The standard curve was obtained by preparing serial dilutions and reading the absorbance at 450 nm.

2.4. Osteogenesis In Vivo. *2.4.1. Implantation.* Six New Zealand white rabbits with a weight of approximately 2.5 kg were employed in the animal experiment, which was approved by the Ethics Committee of West China Hospital at Sichuan University in compliance with all regulatory guidelines. The n-HA/GCO−PU scaffold was cut into sections with a diameter of 7 mm and a length of 6 mm and sterilized by autoclave prior to use. A defect with a size similar to the cylindrical sample was created on both femoral condyles of each rabbit, the scaffold sample was implanted into the defect and the musculature and skin incision were closed with nylon sutures. Each rabbit was given an intramuscular injection of penicillin 1×10^5 units per day during the first 3 days postoperation. The animals were sacrificed via CO_2 asphyxiation, and the samples with surrounding tissue were harvested

DOI: 10.1021/acsami.5b07327
ACS Appl. Mater. Interfaces 2015, 7, 22618−22629

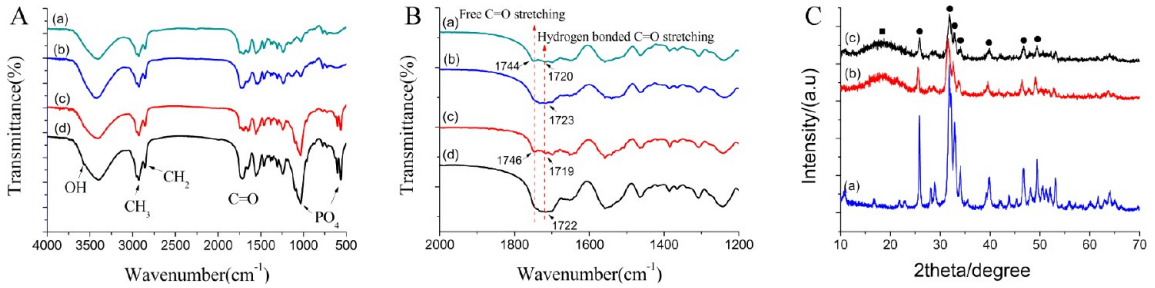

Figure 1. Characterization by (A and B) FT-IR of (a) CO−PU, (b) GCO−PU, (c) n-HA/CO−PU, and (d) n-HA/GCO−PU and by (C) XRD of (a) n-HA, (b) n-HA/CO−PU, and (c) n-HA/GCO−PU; (●) HA crystalline phase and (■) poorly crystallized PU phase.

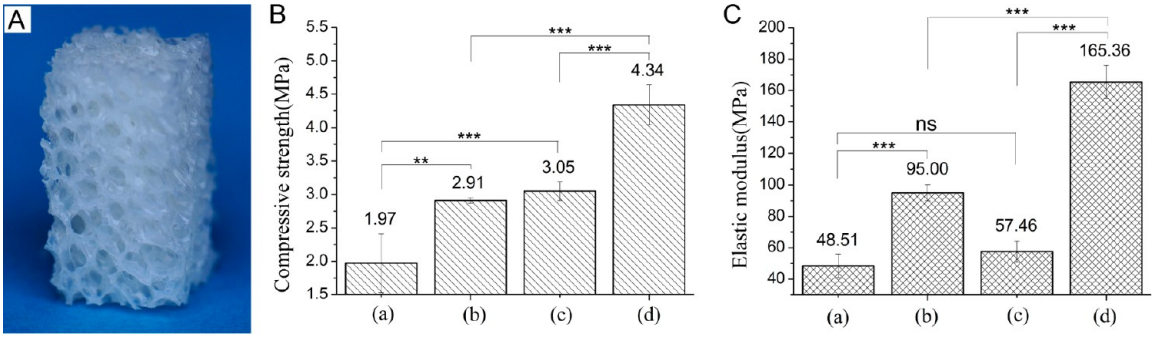

Figure 2. (A) Digital photo, (B) compressive strength, and (C) elastic modulus of scaffolds. For panels B and C: (a) CO−PU, (b) GCO−PU, (c) n-HA/CO−PU, and (d) n-HA/GCO−PU. (Error bars represent standard deviation from the mean (n = 5). (***) $p < 0.001$. (**) $p < 0.01$. (ns) $p > 0.05$.).

at 12 and 24 weeks. Two samples were randomly selected for micro-CT, and four samples were used for histological analysis.

2.4.2. Micro-CT Imaging. Quantitative imaging of new bone tissue was performed using a micro-CT imaging system (μCT40 scanner). A threshold between 450 and 1000 was applied to discriminate the bone tissue, and a threshold between 220 and 450 was applied to discriminate the scaffold, and a 3D Gaussian filter was constrained at σ = 1.2 and support = 2 for partial suppression of the noise in the test volumes. The 3D reconstructed images of the new bone tissue were acquired from a series of 212 serial 2048 × 2048 bitmap images. The obtained micro-CT images were analyzed for the quantitative evaluation of osteogenesis on and in the porous scaffold, which employed the Direct Method software attached to the micro-CT to derive the trabecular number (Tb.N), trabecular thickness (Tb.Th), trabecular separation (Tb.Sp) and bone volume to tissue volume (BV/TV), and bone surface to bone volume (BS/BV). A cylindrical region of interest (ROI) with a diameter of 7 mm and a height of 2 mm was selected to characterize the porous scaffold and the inner regenerated bone. To investigate the distribution of bone growth within the scaffold in three dimensions, we measured the bone occupancy fraction as a function of distance from the scaffold periphery to the scaffold center.

2.4.3. Histological Observation. The harvested samples were fixed in 4% buffered paraformaldehyde, decalcified, dehydrated through gradient ethanol, cleaned in xylene, and embedded with paraffin wax. The samples were cut into sections (thickness of 5 μm) along the sagittal plane, stained with Masson's staining and observed under optical microscopy.

2.5. Statistical Analysis. Quantitative data are presented as the means ± standard deviation (SD). Statistical significance was determined using SPASS (v. 10.0) software. A statistical comparison of the two groups was performed using Student's t test. A difference was considered to be significant when $p < 0.05$.

3. RESULTS

3.1. Chemical Properties of the PU Matrix and n-HA/PU Scaffolds. The chemical structures of the CO−PU and GCO−PU matrixes are presented in Scheme 1, in which more intermolecular hydrogen bonds can be formed in the GCO−PU matrix due to the modification of PU soft segment by polar glyceride of castor oil. The alcoholization of castor oil can effectively provide a greater number of OH groups, and the hydroxyl value increases from 159 of pristine castor oil to 288 of GCO. As shown in Figure 1 (A, B), the absorption bands at 1720 and 1744 cm^{-1} belong to the carbonyl (C═O) stretching of urethane (CONH) groups of the PU matrix. The OH peak at 3571 cm^{-1} and the PO_4 stretching bands at approximately 1033 and 566 cm^{-1} suggest the presence of an n-HA phase in the composite scaffolds. Note that both hydrogen-bonded C═O stretching at 1720 cm^{-1} and free C═O stretching at 1744 cm^{-1} are present in the CO−PU matrix, whereas only hydrogen-bonded C═O stretching at approximately 1723 cm^{-1} appears in the GCO−PU matrix. The n-HA-incorporated PUs exhibit a similar structure. The intensity of the hydrogen-bonded carbonyl peak increases from GCO−PU to n-HA/GCO−PU, and the enhanced intensity of the C═O peak in n-HA/GCO−PU composite indicates the formation of additional hydrogen bonding, which may cause stronger inorganic−organic interface bonding and intermolecular interaction.

The XRD patterns in Figure 1C confirm the presence of a typical HA crystalline phase (●) and a poorly crystallized PU phase (■); no other calcium phosphate or impurity phases were detected. The main characteristic diffraction peaks of n-HA occur at 2θ = 25.9° (002) and 31.9° (211), and PU envelop peak centers occur at approximately 2θ = 19°.

3.2. Compressive Strength and Elastic Modulus of PU and n-HA/PU Scaffolds. All the scaffolds have a macro morphology like that in Figure 2A. The data in Figure 2B,C demonstrate a positive effect of the alcoholization of castor oil and the use of n-HA particles on the mechanical properties of PU scaffolds. When the castor oil is modified by glycerol, the

DOI: 10.1021/acsami.5b07327
ACS Appl. Mater. Interfaces 2015, 7, 22618−22629

compressive strength of the GCO−PU scaffold increases to 2.91 MPa, which is significantly higher than the 1.97 MPa of the CO−PU scaffold (increased by 48%), and the elastic modulus is increased by 96%, from 48.51 to 95 MPa. When n-HA particles are incorporated, both the strength and the modulus of n-HA/PU composite scaffolds are distinctly enhanced. The compressive strength (4.34 MPa) and elastic modulus (165.36 MPa) of the n-HA/GCO−PU scaffold are considerably higher than the compressive strength and elastic modulus of the GCO−PU scaffold and n-HA/CO−PU scaffold. The results in Figure 2B,C indicate that both the modification of the PU matrix and the incorporation of n-HA filler can improve the mechanical properties of PU scaffolds. The comparison of the four scaffolds indicates that modification of the PU matrix has a greater contribution to the elastic modulus and incorporation of n-HA filler has a greater contribution to the compressive strength, as shown in Figure 2B,a−c and C,a−c. However, the combination of the two factors yields greater improvement (Figure 2B,d and C,d), which suggests the important role of the bonding interface between n-HA particles and the GCO−PU matrix.

The porosity of the scaffolds is listed in Table 1. In general, the porosity of the four scaffolds is approximate; the CO−PU scaffold shows a minimum value (52.90%). A slightly higher porosity can be observed after the use of the GCO−PU matrix and n-HA particles, which should be driven by a more sufficient reaction and foaming process during GCO−PU polymerization and a larger pore nucleation site provided by n-HA particles.

Table 1. Porosity of Scaffolds

sample	porosity (%)
CO−PU	52.90 ± 2.26
GCO−PU	56.38 ± 3.72
n-HA/CO−PU	54.46 ± 5.68
n-HA/GCO−PU	57.14 ± 2.02

3.3. Chemical Mechanisms of CO−PU and GCO−PU. The XPS spectra of CO−PU and GCO−PU scaffolds are shown in Figure 3A,B. The substitution of GCO for CO significantly increases the binding energy of the HN-CO-O group, especially the CO−N−CO group. The related binding energy and peak area calculated from the fit of the high-resolution XPS spectra are listed in the top right of Figure 3A,B. The main peak of HN-CO-O and the small peak of CO−N−CO for the CO−PU scaffold appear at 399.21 and 399.96 eV, respectively, and are derived from allophanate and biuret (Scheme 1(C, D)), which are created by the reaction of residual IPDI with urethane and foaming agent water. The bonding energy of CO−N−CO for the GCO−PU scaffold is increased to 402.35 eV compared with 399.96 eV for the CO−PU scaffold, which indicates a stronger hydrogen interaction and a more stable network system. Note that the peak area or molar concentration of the CO−N−CO group significantly enhances from 19.36% of CO−PU to 25.99% of GCO−PU, which is driven by the weaker reaction inhibition, namely, the highly active GCO segments. The evolution of storage modulus (E') as a function of temperature measured by DMA is shown in Figure 3C. The E′ value of GCO−PU is higher compared to the E' value of CO−PU. The more OH groups of GCO−PU can help to improve the cross-linking degree.

3.4. Chemical Mechanisms of n-HA/PU. The XPS spectra of n-HA/PU scaffolds are shown in Figure 4(A, B). The peak area of CO−N−CO group increases from 14.54% of n-HA/CO−PU to 19.93% of n-HA/GCO−PU, which reveals a similar but smaller trend than that of the CO−PU and GCO−PU scaffolds. The OH groups of the n-HA particles may react with IPDI and cause the decline of CO−N−CO group.

The solid ^{13}C NMR spectra of the n-HA/CO−PU and n-HA/GCO−PU scaffolds are displayed in Figure 4(D and E). The peaks observed at 172 ppm (C-a) and from 157 to 160 ppm (C-e) represent the hydrogen-bonded C═O and the urethane linkage, respectively, that are produced by the reaction between the ester group and the hydroxyl functional group. The signals at 132 ppm (C-b) and 125 ppm (C-c) are attributed to the alkene groups in castor oil. The peak at 73 ppm is assigned to methylidyne carbon adjacent to urethane (C-d). The peak at 69 ppm (C-f) relates to the hard-segment carbons adjacent to the amino group. The peaks at approximately 45 ppm are associated with the methylene of the six-membered ring in IPDI, and the peaks ranging from 11 to 40 ppm belong to the saturated fatty carbons in both the soft segments and the hard segments. Stronger peak intensity, which is representative of urethane and biuret from approximately 157−158 ppm and representative of the hard-segment carbons adjacent to the amino group at 69 ppm, can be observed for the n-HA/GCO−PU scaffold in Figure 4E compared with the n-HA/CO−PU scaffold in Figure 4D.

The evolution of the storage modulus (E') as a function of temperature, as measured by DMA, is shown in Figure 4C. The E′ value of the n-HA/GCO−PU composite is higher than the E′ value of the n-HA/CO−PU composite. The temperature of the initial rapid decrease of the storage modulus, which is produced from an increase in molecular mobility with temperature, is approximately 25 °C for n-HA/CO−PU and 45 °C for n-HA/GCO−PU. The results indirectly indicate that the GCO−PU matrix has a higher cross-linking density. Both the enhanced cross-linking and the interface interaction

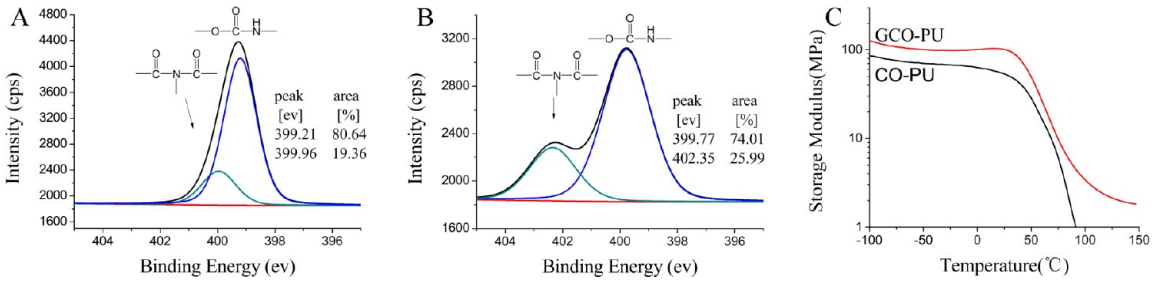

Figure 3. N 1s XPS spectra of scaffolds: (A) CO−PU and (B) GCO−PU. The main peak of HN-CO-O represents urethane, and the small peak of CO−N−CO derives from allophanate and biuret. (C) Storage moduli of PU as a function of temperature.

DOI: 10.1021/acsami.5b07327
ACS Appl. Mater. Interfaces 2015, 7, 22618−22629

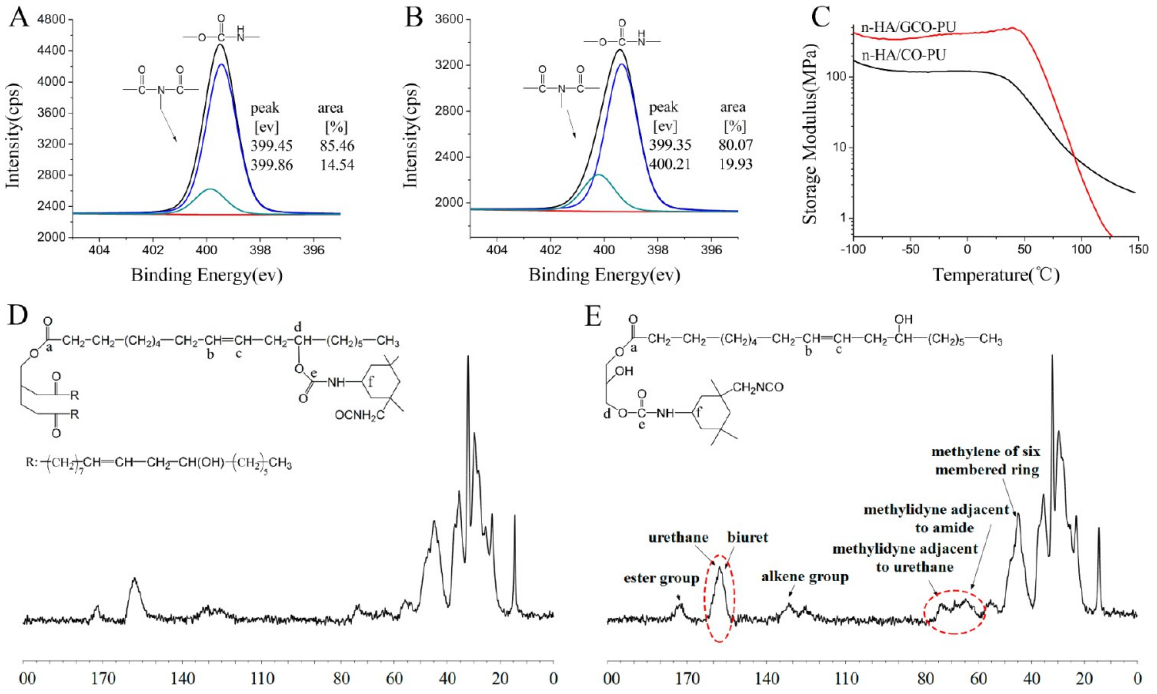

Figure 4. (A and B) N 1s XPS spectra of scaffolds and (D and E) characterization by ^{13}C NMR: (A and D) n-HA/CO−PU and (B and E) n-HA/GCO−PU. (C) Storage moduli of n-HA/PU composites as a function of temperature.

between the n-HA particles and the GCO−PU matrix facilitate the increased storage modulus.

3.5. Interface Structure of n-HA/GCO−PU. The TEM micrographs in Figure 5 reveal the distribution of n-HA particles in the GCO−PU matrix (A, B), the interface of n-HA and GCO−PU (C) and the hard−soft segments of the GCO−PU matrix (D). A uniform dispersion of n-HA particles in the GCO−PU matrix and tightly interfacial bonding are visible, and the n-HA particles have a rod-shaped morphology with a length that ranges from approximately 50−100 nm and a width of 20 nm. No interface gap or phase separation is present.

PU is biphasic due to the presence of soft and hard segments.[27] When the PU matrix is stained by ruthenium tetroxide (RuO_4),[26] its two phases are represented by different colors on the high-resolution TEM images. As shown in Figure 5D, the soft (black) segment and hard (white) segment of the PU matrix exhibit a nanodomain, that is, nanospots or elongated nanorods that are highly interpenetrated. The gray interphase should reflect the "bridge" between the hard segment and the soft segment.

To verify the positive effect of nano-HA particles on mechanical quality, we also used micro-HA particles to construct the μ-HA/PU scaffolds. In Figure 6A, the compressive strength of the μ-HA/GCO−PU scaffold is 2.40 MPa, which is slightly higher than the compressive strength of 2.23 MPa of the μ-HA/CO−PU scaffold, and the elastic modulus increases from 20.86 to 40.81 MPa. However, the compressive strength and the elastic modulus of the μ-HA/CO−PU and μ-HA/GCO−PU scaffolds are considerably lower than the compressive strength and the elastic modulus of the n-HA/CO−PU and n-HA/GCO−PU scaffolds and even lower than the compressive strength and the elastic modulus of the pure CO−PU and GCO−PU scaffolds, with the exception that the compressive strength of μ-HA/CO−PU is slightly higher than the compressive strength of CO−PU scaffold (1.91 MPa). As shown in the XPS spectra in Figure 6B,C, the peak area of CO−N−CO substantially declines to 6.52% (μ-HA/CO−PU) and 7.70% (μ-HA/GCO−PU), which produces a weak cross-linking intensity. According to the SEM and TEM micrographs in Figure 6D−F, the spherical μ-HA particles of approximately 5−15 μm randomly distribute in the CO−PU (D) and GCO−PU (E) matrixes, which shows a distinct interface gap or loose interface bonding. This behavior indicates that the μ-HA particles will hinder the stress transfer and intermolecular interaction. Compared with the μ-HA particles, the use of n-HA particles and GCO−PU matrix can endow the n-HA/GCO−PU scaffold with a tightly bonded interface, a stable composite structure and improved mechanical quality. The possible mechanism is presented in Figure 7. In the CO−PU matrix (A), dangling and unreacted end groups (within red circles) of castor oil remain due to low activity, which weakens the mechanical strength of the PU matrix. In the GCO−PU matrix (B), abundant covalent cross-links can form between hard segments (purple cuboid) and soft segments (black zigzag line) due to the short chain and high activity of alcoholized castor oil, which improves the mechanical quality of the matrix. In the n-HA/GCO−PU composite (C), n-HA particles (yellow cuboid) with uniform dispersity are chemically bonded with the GCO−PU matrix and modify the polymer network dynamics.

3.6. Cytocompatibility of the n-HA/GCO−PU Scaffold In Vitro. As a result of its outstanding mechanical properties, a biological evaluation was performed by directing the evaluation to the n-HA/GCO−PU composite scaffold. The digital photo and micro-CT reconstructed image of the scaffold are shown in Figure 8A,B. The scaffold appears spongy and exhibits an interconnected pore structure with macropores penetrated by small pores, in which the majority of the pores range from 200 to 800 μm. The ability of the scaffold to support the proliferation and osteogenic differentiation of the MSCs is presented in Figure 8C−F. After seeding for 4 days, the MSCs have adhered to the surface of the n-HA/GCO−PU scaffold, as observed by the SEM photo and the live/dead staining image in

DOI: 10.1021/acsami.5b07327
ACS Appl. Mater. Interfaces 2015, 7, 22618−22629

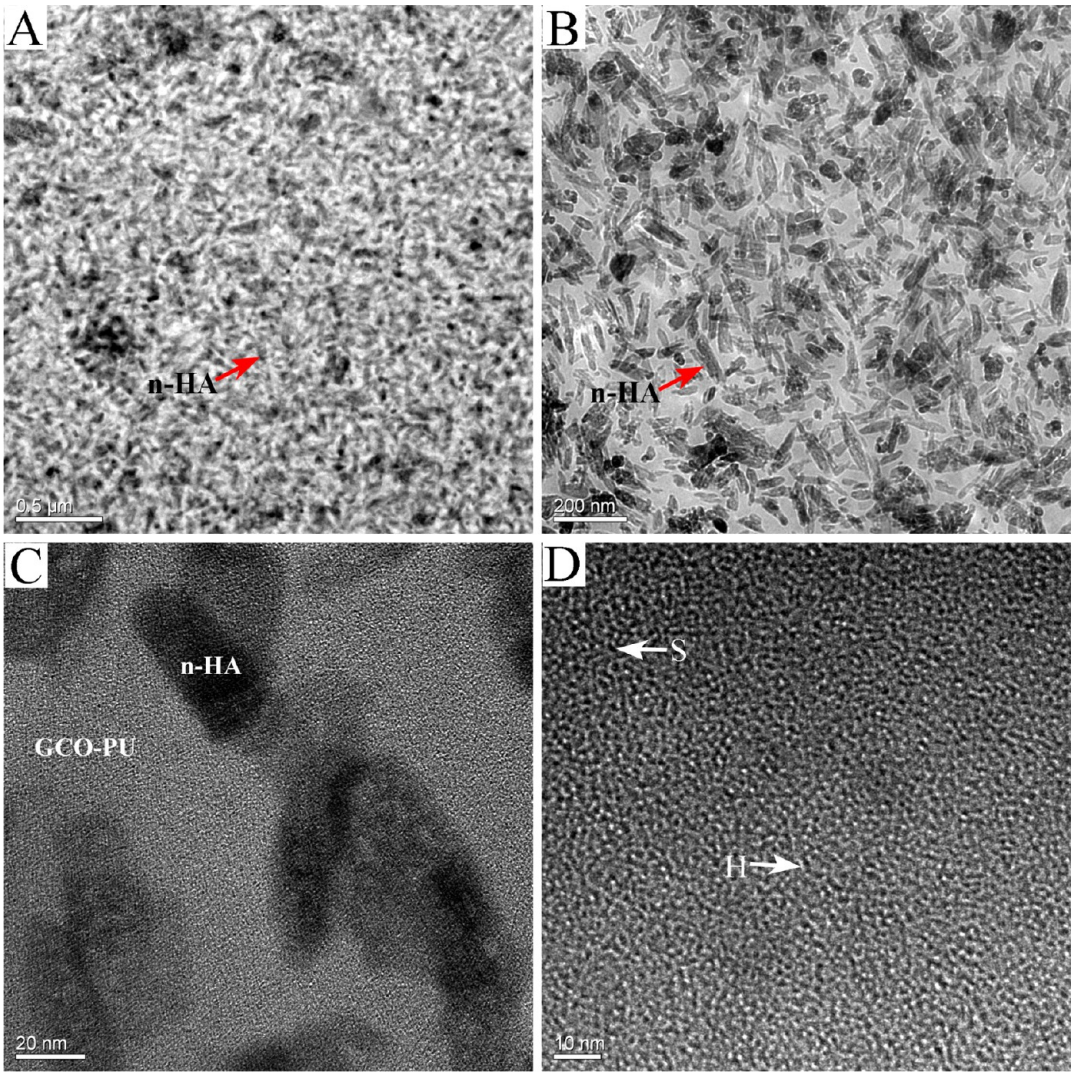

Figure 5. (A and B) TEM micrographs of n-HA/GCO−PU composite, (C) HRTEM images of the n-HA and GCO−PU interface, and (D) the ruthenium tetroxide stained GCO−PU matrix: soft segments (S, in black), hard segments (H, in white) and interphase (gray).

Figure 8C,D. The cells exhibit a normal polygonal and elongated shape and limited intercellular communication. On day 11, a cell layer has formed on the scaffold surface and the cells grow also in the scaffold porous structure and spread with numerous filopodia, lamellipodia and cytoplasmic extensions. As shown in Figure 8E, the cell viability or proliferation continuously increases with culture time. No significant difference between the control group and the n-HA/GCO−PU scaffold is observed prior to day 7; however, the scaffold cell viability increases at a significantly higher rate than the control on day 11 ($p < 0.001$). The osteocalcin (OCN) expression in Figure 8F confirms the increasing trend because the OCN level of n-HA/GCO−PU scaffold steadily increases at a higher rate than the control over a period of 11 days. These results demonstrate that the n-HA/GCO−PU scaffold has excellent cytocompatibility and is a suitable template for MSC attachment, growth, proliferation and osteogenic differentiation.

3.7. Osteogenesis of the n-HA/GCO−PU Scaffold in Vivo. The 3D micro-CT reconstructed images in Figure 9A,C present the mineralized regenerated bone tissue in the surface region and within the pores of the n-HA/GCO−PU scaffold. New bone with high density has formed in the surface region, and a bone matrix and trabecula have also grown into the scaffold porous structure. The quantity of new bone at 24 weeks is substantially greater than the quantity of new bone at 12 weeks. The bone ingrowth volume fraction in Figure 9B,D shows the distribution of new bone from the scaffold periphery to the scaffold center. The curves demonstrate that the regenerated new bone preferentially forms on the surface and subsequently grows inward following an osteoconductive pathway.

Detailed information about the tissue volume parameters is listed in Table 2. The bone volume density (bone volume/tissue volume, BV/TV) significantly increases with time. Conversely, the bone surface density (bone surface area/bone volume, BS/BV) shows a downward trend, which indicates that the new bone tissue has gradually thickened by growing into the scaffold porous structure. The increase in the trabecular thickness (Tb.Th) and the trabecular number (Tb.N) as well as the decline of the trabecular separation (Tb.Sp) also confirm the progress of bone regeneration.

The histological sections of the n-HA/GCO−PU scaffold samples after implantation into the femoral condyle of rabbits for 12 and 24 weeks are shown in Figure 10. The Masson stained new bone matrix is shown in blue and dark red. The

DOI: 10.1021/acsami.5b07327
ACS Appl. Mater. Interfaces 2015, 7, 22618−22629

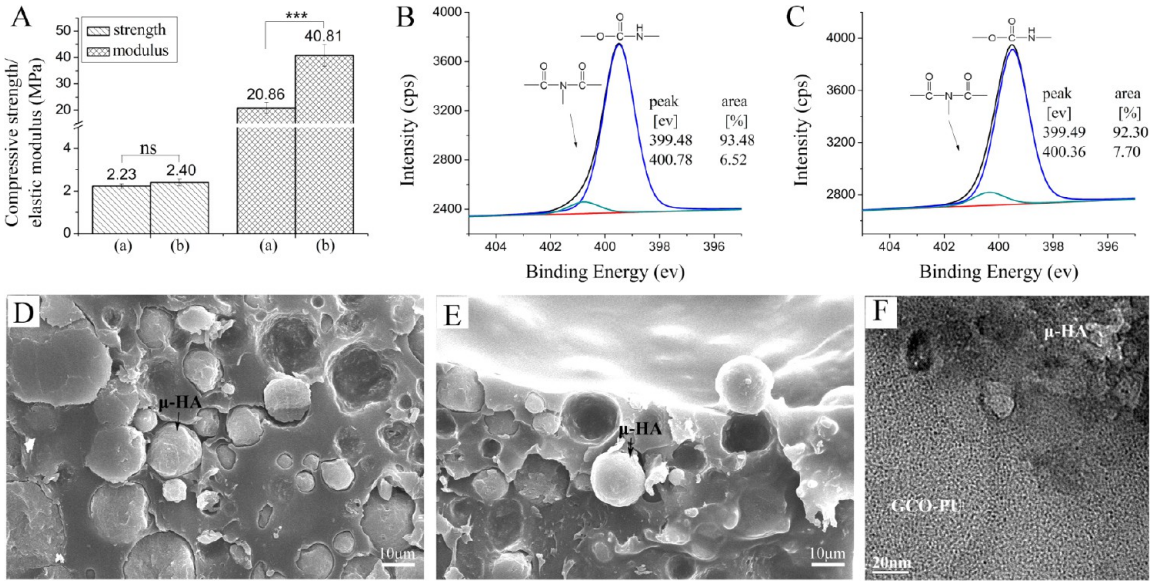

Figure 6. (A) Mechanical properties of (a) μ-HA/CO−PU and (b) μ-HA/GCO−PU; XPS spectra of (B) μ-HA/CO−PU and (C) μ-HA/GCO−PU; SEM micrographs of (D) μ-HA/CO−PU and (E) μ-HA/GCO−PU composites; (F) HRTEM images of μ-HA/GCO−PU. Error bars represent standard deviation from the mean (n = 5); (***) $p < 0.001$, (ns) $p > 0.05$..

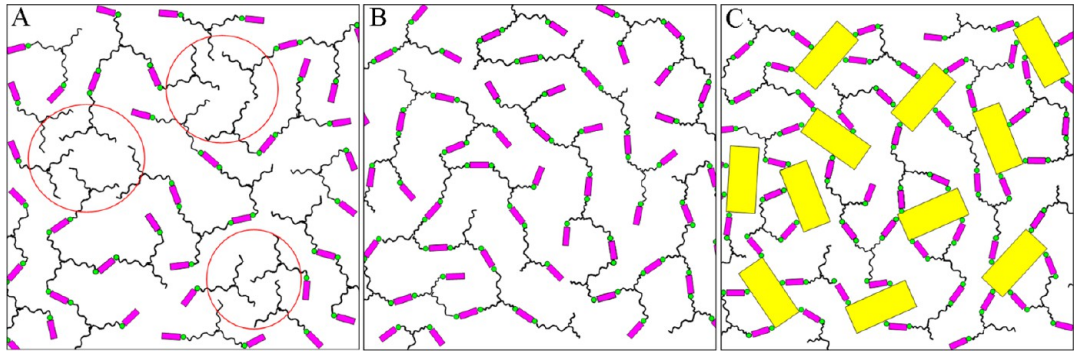

Figure 7. Schematic of three mechanisms that determine the mechanical properties for the (A) CO−PU matrix (dangling unreacted end groups within red circles), (B) GCO−PU matrix (abundant covalent cross-links), and (C) n-HA/GCO−PU composite (well-dispersed n-HA particles bonding with the GCO−PU matrix); (purple cuboid) hard segments, (black zigzag line) soft segments, (yellow cuboid) n-HA particles, and (green dot) covalent bond.

regenerated new bone shows a dense organized matrix. The new bone tissue forms not only on the contact interface of the scaffold and the native bone, but also in the scaffold porous structure through the interconnected pore channel. Bone tissue is observed along the pore wall and tightly integrates with the scaffold inner surface. Especially at 24 weeks, new bone has nearly grown throughout the entire scaffold and formed a connected structure.

4. DISCUSSION

A biomaterial with a porous structure favors tissue ingrowth, mass transportation of nutrients, osteointegration with host bone, and long-term stable fixation of bone implants.[28,29] To promote mechanical properties and bone tissue regeneration, the design of our n-HA/GCO−PU scaffold has considered the hierarchical structure, including the molecular modification of PU soft segment, the introduction of nano-HA particles, and the formation of porous structure. On a microscale, a porous structure with a pore size of approximately 200−800 μm and a porosity of 57% are appropriate for the growth of cells (Figure 8) and the regeneration of bony tissues (Figure 9). On a nanoscale, the introduction of n-HA particles not only improves the dispersity (Figure 5B) and the interface bonding with the GCO−PU matrix (Figure 5C) but also provides effective bioactivity to bond with bone tissue (Figure 10). Equally important is the dimension of the segment domains, especially the nanodomain of the hard and soft segments in the GCO−PU matrix (Figure 5D). This unique hierarchical structure can be considered to be similar to the segmented collagen, the nanoscale apatite mineral phase that is incorporated in the organic matrix, and the cancellous structure of natural bone, which can be crucial for high-performance scaffolds that are employed for bone repair and regeneration.

The compressive strength and elastic modulus of the n-HA/GCO−PU scaffold are considerably higher than the compressive strength and elastic modulus of reported PU/bioglass porous composite and other PU/HA scaffolds.[13,16] Despite the high compressive strength of ceramic scaffolds, their brittleness and too high elastic modulus comparing to bone limit their application in bone tissue engineering.[30,31] The mechanical quality of porous composites can be determined by the properties of the organic matrix, the mineral structure, and the

DOI: 10.1021/acsami.5b07327
ACS Appl. Mater. Interfaces 2015, 7, 22618−22629

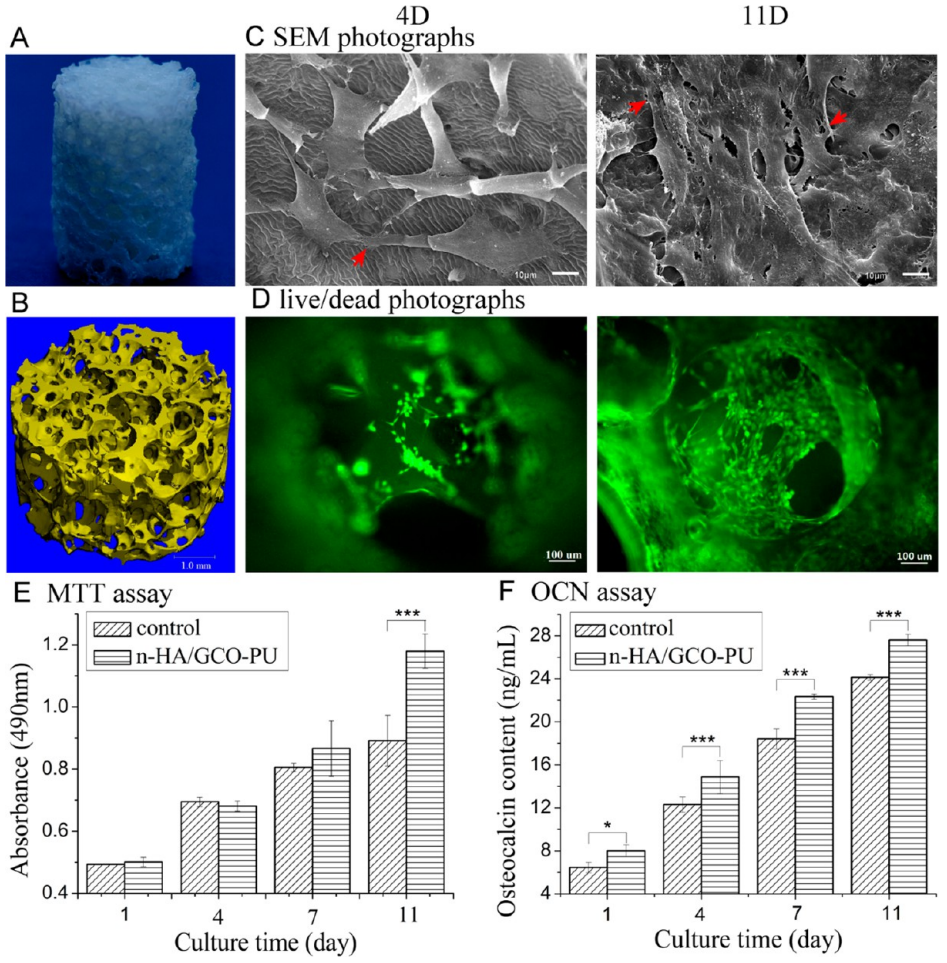

Figure 8. Digital photo (A) and micro-CT reconstructed image (B) of n-HA/GCO−PU scaffold; SEM photographs (C) and fluorescence images (D); arrows denote the cell's stretched pseudopodia, 4D-culture for 4 days, 11D-culture for 11 days; (E) MTT assay for the proliferation and (F) OCN assay of MSCs cultured with n-HA/GCO−PU for 1, 4, 7, and 11 day(s) compared with the blank control (tissue culture plastic) for the same culture condition. Error bars represent the standard deviation from the mean (n = 4); (***) $p < 0.001$, (*) $p < 0.05$.

geometrical arrangement of the two components.[22,32−34] The intermolecular cross-linking provides fibrillar matrices with various mechanical properties for the organic matrix of bone.[35] Because polyurethane is a block copolymer with hard and soft segments, its phase behavior can be mapped onto the well-known block copolymer phase diagram.[26,36,37] As a result, the distribution of the soft and hard segments of a PU matrix is speculated to be arranged as shown in Figure 7A,B, which is dependent on the segment length and the interaction between the hard and soft segments. The GCO−PU matrix shows a finely arranged network structure. The comparison with pristine castor oil indicates that the increased hydroxyl number of GCO can enhance its polymerization reaction with isocyano of IPDI, which produces a higher cross-linking density of the GCO−PU network. The urethane in GCO−PU can easily react with residual IPDI; thus, the presence of GCO facilitates the interaction force between the hard and soft segments, and the mechanical properties are enhanced. The higher peak area and bonding energy (Figure 3B) of the CO−N−CO group of the GCO−PU matrix is evidence of the increase in the cross-linking density and a more stable network system, which is consistent with the E' value of GCO−PU (Figure 3C). Due to the higher hydroxyl number of the GCO group and the polarity of the GCO−PU matrix, the GCO−PU matrix is capable of more types of interactions within its molecular chains, such as hydrogen bonding (Scheme 1B and Figure 1B) and polar−polar interactions (as with urethane). Conversely, the dangling chain and the unreacted end groups of pristine castor oil (Figure 7A) will decrease the cross-linking density and weaken the mechanical strength of the PU matrix.

The size, shape, and arrangement of the mineral particles play a pivotal role in defining the mechanical properties of a composite,[38] as supported by the results of our experiment. The n-HA particles with a nanosize and rod shape enhance the mechanical properties of HA/PU scaffolds compared with the μ-HA/PU scaffolds, which may be attributed to the small size effect, the high surface activity, the uniform distribution in the PU matrix, and the close interface bonding. The hydrophilic n-HA particles should preferentially bond with the polar hard segments instead of the nonpolar CO segments of the PU matrix; which endows the n-HA/GCO−PU scaffold with good mechanical performance. The FT-IR spectra (Figure 1B) confirm that the GCO−PU matrix experiences less free C═O stretching compared with the CO−PU matrix, and the enhancement of the hydrogen-bonding carbonyl peak at 1722 cm^{-1} in the n-HA/GCO−PU scaffold indicates the formation of stronger hydrogen bonding, which generates stronger intermolecular and interfacial interaction. The N 1s XPS spectra in Figure 4B show that the CO−N−CO peak area of the n-HA/GCO−PU scaffold is larger than that of the n-HA/

DOI: 10.1021/acsami.5b07327
ACS Appl. Mater. Interfaces 2015, 7, 22618−22629

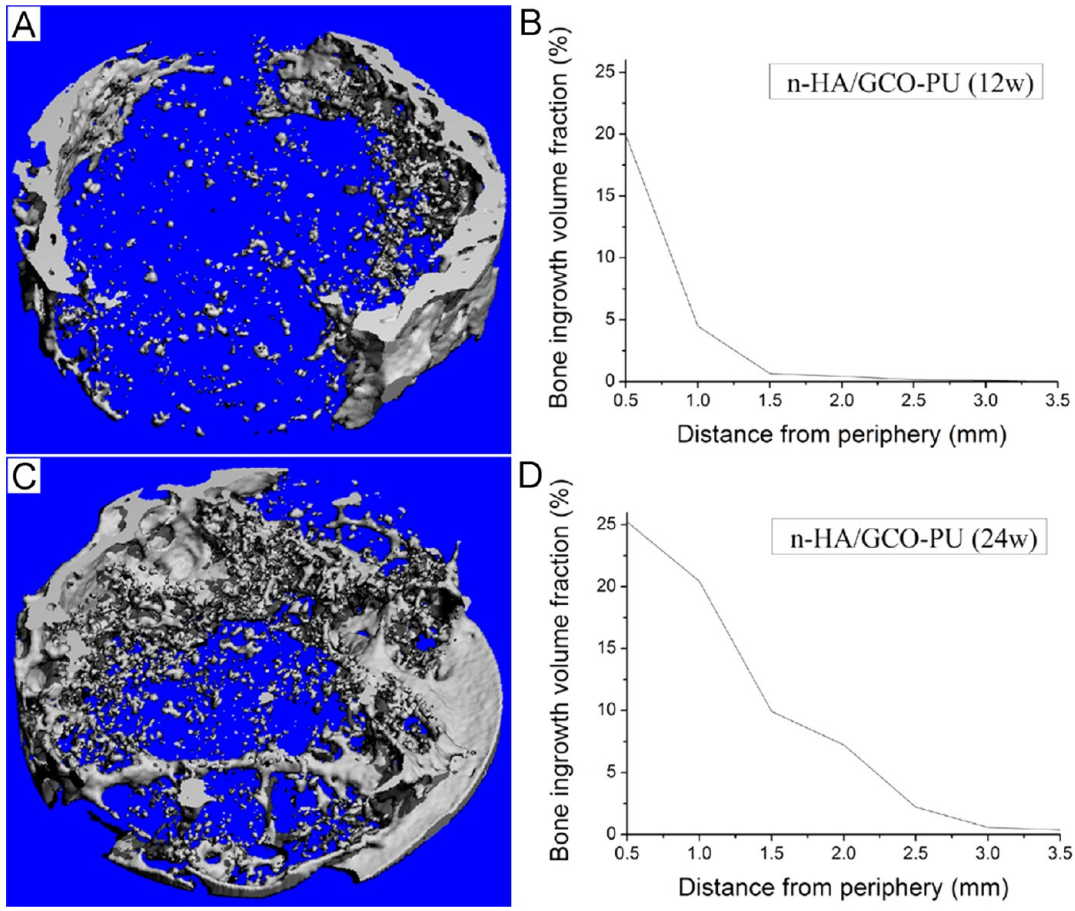

Figure 9. (A and C) Regenerated bone tissue reconstructed by the 3D micro-CT image after removal of the n-HA/GCO−PU scaffold and (B and D) bone ingrowth volume fraction as a function of distance from the scaffold periphery to the scaffold center at (A and B) 12 and (C and D) 24 weeks.

Table 2. Summary of New Bone Formation inside the Porous n-HA/GCO−PU Scaffold[a]

sample	Tb.Th (mm)	Tb.Sp (mm)	Tb.N (mm)	BV/TV (%)	BS/BV (mm^2/mm^3)
n-HA/GCO−PU (12 W)	0.162	0.777	1.34	6.32	18.3
n-HA/GCO−PU (24 W)	0.219	0.608	1.68	14.3	15.5

[a]Tb.Th: trabecular thickness; Tb.Sp: trabecular separation; Tb.N: trabecular number; BV/TV: bone volume/tissue volume; BS/BV: bone surface/bone volume.

CO−PU scaffold. The NMR spectrum (Figure 4E) also shows stronger urethane and biuret peaks at approximately 157−158 ppm, and stronger peak of the hard-segment carbons adjacent to the amino group at 69 ppm, due to more OH groups and less steric hindrance of n-HA/GCO−PU composite. These changes are closely related to the hydrogen bonds between the soft and hard segments and between the n-HA particles and the GCO−PU matrix. The terminal −NCO groups may react with the −OH groups of n-HA and form a urethane linkage. This phenomenon corresponds with the findings reported by Khan et al.[39] The binding energy position of same chemical group could be different in CO−PU, GCO−PU, n-HA/CO−PU, n-HA/GCO−PU, μ-HA/CO−PU, and μ-HA/GCO−PU because the chemical environment of the six samples should be different. For example, the GCO has more −OH groups than CO to react with the −NCO groups, the specific surface area and surface activity of n-HA are higher than μ-HA, and the surface −OH group of HA will also affect the chemical reaction between −OH and −NCO of IPDI. Thus, the stronger intermolecular interaction, small size effect of the n-HA filler and the tightly bonded interface become the three dominating factors for mechanical improvement of an n-HA/GCO−PU scaffold. These factors may prove helpful for future designs of high-performance composite biomaterials.

Another reason for the high strength of the nanocomposite may be the delay of the fracture process caused by n-HA particles because the large particle size and the poor interface state of μ-HA particles will restrict the transition of stress. The spherical μ-HA particles reveal a distinct interface gap in the PU matrix (Figure 6D,E). Conversely, the n-HA particles are closely bonded to the PU matrix and no gap or phase separation is present (Figure 5B,C). The uniform dispersion of n-HA particles in the PU matrix may produce a vast number of interfacial regions, which may strengthen the PU matrix by reducing slippage during straining. Due to the synergistic effect of n-HA and GCO or GCO−PU, both the compressive strength and the elastic modulus of the n-HA/GCO−PU scaffold are markedly improved.

The cell culture results, including the MTT and OCN assays (Figure 8), demonstrate that the n-HA/GCO−PU porous scaffold can promote cell adhesion, spreading, proliferation and osteogenic differentiation. In addition to superior biocompatibility, the mechanical quality of a scaffold plays an important

DOI: 10.1021/acsami.5b07327
ACS Appl. Mater. Interfaces 2015, 7, 22618−22629

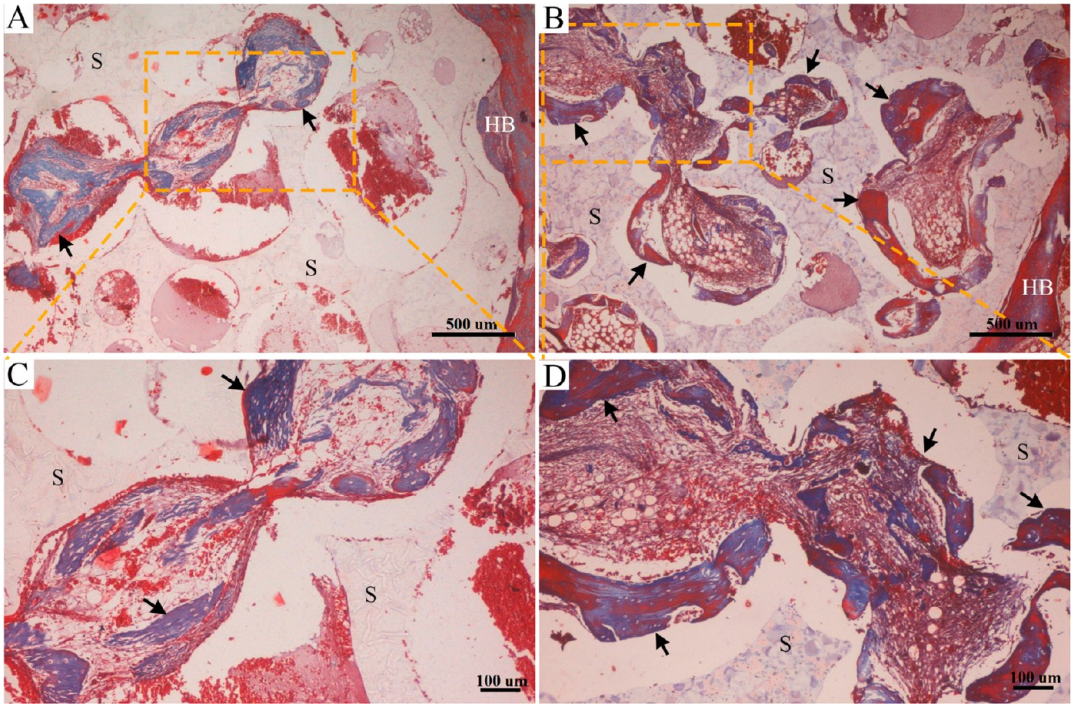

Figure 10. Masson's stained histological sections of n-HA/GCO−PU scaffold implanted for (A and C) 12 and (B and D) 24 weeks; S, scaffold; HB, host bone; black arrows, new bone.

role in bone reconstruction.[40−42] The compressive strength (4.34 MPa) and elastic modulus (165.36 MPa) of the n-HA/GCO−PU scaffold are considerably higher than the compressive strengths and elastic moduli of pure PU, n-HA/CO−PU and μ-HA/PU scaffolds and are equivalent to the compressive strength and elastic modulus of cancellous bone (mechanical strength >2 MPa, Young's modulus >0.05 GPa),[5] which can prevent stress mismatch at the bone/scaffold interface and provide appropriate mechanical support for new bone regeneration. The osteogenesis capacity of the n-HA/GCO−PU scaffold was evaluated in the femoral condyle defects of rabbits. The 3D micro-CT analysis exhibits good bone regeneration and reconstruction with time, and bone growth from the scaffold periphery to the scaffold center (Figure 9). The Masson stained histological sections demonstrate the growth of new bone into the porous structure and bonding with the scaffold's outer and inner surfaces (Figure 10). The n-HA/GCO−PU porous scaffold has the ability to guide new bone formation, which causes successful bone regeneration and scaffold/bone integration.

5. CONCLUSION

Polyurethane is an elastomer with mechanical properties that are adjustable by polymerizing different soft and hard segments and blending with inorganic fillers. The selection of its building blocks, the modification of its soft segment by alcoholized castor oil, and the incorporation of n-HA particles in its matrix provide effective enhancements, according to the results of this experiment. We found that the use of glyceride of castor oil for soft segments and the incorporation of n-HA particles are crucial for the mechanical improvement of PU-based composite scaffolds and that the scaffold composition, porous structure and mechanical quality are favorable for cell proliferation and new bone regeneration. The modification of the PU matrix by glyceride of castor oil has a considerable effect on the elastic modulus, whereas the incorporation of n-HA filler has a greater effect on the compressive strength. The combination of the two factors yields distinct mechanical improvement, which suggests the important role of the tightly bonded interface between the n-HA particles and the PU matrix. The nano-to-micro hierarchical structure and the improved mechanical properties of the nanoscale composite scaffold can be a biomimetic approach to natural bone tissue, to produce strong vitality in bone regeneration and reconstruction.

AUTHOR INFORMATION

Corresponding Authors

*E-mail: nic7504@scu.edu.cn.
*E-mail: zoae@scu.edu.cn.
*E-mail: zouqin80913@126.com.

Notes

The authors declare no competing financial interest.

ACKNOWLEDGMENTS

The authors appreciate the financial support from the China NSFC fund (No. 31370971), the China national 863 project (2013AA032203) and the Sichuan and Chengdu project (No. 2012FZ0125, 12DXYB145JH-005).

REFERENCES

(1) Wu, S.; Liu, X.; Yeung, K. W. K.; Liu, C.; Yang, X. Biomimetic Porous Scaffolds for Bone Tissue Engineering. *Mater. Sci. Eng., R* **2014**, *80*, 1−36.
(2) Mayer, G. Rigid Biological Systems as Models for Synthetic Composites. *Science* **2005**, *310*, 1144−1147.
(3) Meyers, M. A.; Chen, P.; Lin, A. Y.; Seki, Y. Biological Materials: Structure and Mechanical Properties. *Prog. Mater. Sci.* **2008**, *53*, 1−206.
(4) Weiner, S.; Wagner, H. D. The Material Bone: Structure-Mechanical Function Relations. *Annu. Rev. Mater. Sci.* **1998**, *28*, 271−298.

DOI: 10.1021/acsami.5b07327
ACS Appl. Mater. Interfaces 2015, 7, 22618−22629

(5) Hench, L. L. *An Introduction to Bioceramic*; Imperial College Press: London, 2013; pp 287−288.
(6) Reznikov, N.; Shahar, R.; Weiner, S. Bone Hierarchical Structure in Three Dimensions. *Acta Biomater.* **2014**, *10*, 3815−3826.
(7) Dawson, J. I.; Oreffo, R. O. Clay: New Opportunities for Tissue Regeneration and Biomaterial Design. *Adv. Mater.* **2013**, *25*, 4069−4086.
(8) Bechtle, S.; Ang, S. F.; Schneider, G. A. On the Mechanical Properties of Hierarchically Structured Biological Materials. *Biomaterials* **2010**, *31*, 6378−6385.
(9) Zuidema, J.; van Minnen, B.; Span, M. M.; Hissink, C. E.; van Kooten, T. G.; Bos, R. In vitro Degradation of A Biodegradable Polyurethane Foam, Based on 1,4-butanediisocyanate: A Three-Year Study at Physiological and Elevated Temperature. *J. Biomed. Mater. Res., Part A* **2009**, *90A*, 920−930.
(10) da Silva, G. R.; da Silva-Cunha, A.; Behar-Cohen, F.; Ayres, E.; Oréfice, R. L. Biodegradation of Polyurethanes and Nanocomposites to Non-Cytotoxic Degradation Products. *Polym. Degrad. Stab.* **2010**, *95*, 491−499.
(11) Zanetta, M.; Quirici, N.; Demarosi, F.; Tanzi, M. C.; Rimondini, L.; Fare, S. Ability of Polyurethane Foams to Support Cell Proliferation and the Differentiation of MSCs into Osteoblasts. *Acta Biomater.* **2009**, *5*, 1126−1136.
(12) Sartori, S.; Chiono, V.; Tonda-Turo, C.; Mattu, C.; Gianluca, C. Biomimetic Polyurethanes in Nano and Regenerative Medicine. *J. Mater. Chem. B* **2014**, *2B*, 5128−5144.
(13) Boissard, C.; Bourban, P.; Tami, A.; Alini, M.; Eglin, D. Nanohydroxyapatite/Poly(ester urethane) Scaffold for Bone Tissue Engineering. *Acta Biomater.* **2009**, *5*, 3316−3327.
(14) Baino, F.; Verne, E.; Vitale-Brovarone, C. Feasibility, Tailoring and Properties of Polyurethane/Bioactive Glass Composite Scaffolds for Tissue Engineering. *J. Mater. Sci.: Mater. Med.* **2009**, *20*, 2189−2195.
(15) Mi, H.; Palumbo, S.; Jing, X.; Turng, L. S.; Li, W.; Peng, X. Thermoplastic Polyurethane/Hydroxyapatite Electrospun Scaffolds for Bone Tissue Engineering: Effects of Polymer Properties and Particle Size. *J. Biomed. Mater. Res., Part B* **2014**, *102*, 1434−1444.
(16) Wang, L.; Li, Y.; Zuo, Y.; Zhang, L.; Zou, Q.; Cheng, L.; Jiang, H. Porous Bioactive Scaffold of Aliphatic Polyurethane and Hydroxyapatite for Tissue Regeneration. *Biomed. Mater.* **2009**, *4*, 025003.
(17) Vasile, E.; Popescu, L. M.; Piticescu, R. M.; Burlacu, A.; Buruiana, T. Physico-Chemical and Biocompatible Properties of Hydroxyapatite Based Composites Prepared by An Innovative Synthesis Route. *Mater. Lett.* **2012**, *79*, 85−88.
(18) Gao, H. Application of Fracture Mechanics Concepts to Hierarchical Biomechanics of Bone and Bone-like Materials. *Int. J. Fract.* **2006**, *138*, 101−137.
(19) Sonnenschein, M. F.; Ginzburg, V. V.; Schiller, K. S.; Wendt, B. L. Design, Polymerization, and Properties of High Performance Thermoplastic Polyurethane Elastomers From Seed-Oil Derived Soft Segments. *Polymer* **2013**, *54*, 1350−1360.
(20) Du, J.; Zou, Q.; Zuo, Y.; Li, Y. Cytocompatibility and osteogenesis Evaluation of HA/GCPU Composite as Scaffolds for Bone Tissue Engineering. *Int. J. Surg.* **2014**, *12*, 404−407.
(21) Gogolewski, S.; Gorna, K.; Zaczynska, E.; Czarny, A. Structure-Property Relations and Cytotoxicity of Isosorbide-Based Biodegradable Polyurethane Scaffolds for Tissue Repair and Regeneration. *J. Biomed. Mater. Res., Part A* **2008**, *85*, 456−465.
(22) Fratzl, P.; Gupta, H. S.; Paschalis, E. P.; Roschger, P. Structure and Mechanical Quality of the Collagen-Mineral Nano-Composite in Bone. *J. Mater. Chem.* **2004**, *14*, 2115−2123.
(23) Yubao, L.; De Wijn, J.; Klein, C. P. A. T.; Van De Meer, S.; De Groot, K. Preparation and Characterization of Nanograde Osteoapatite-Like Rod Rrystals. *J. Mater. Sci.: Mater. Med.* **1994**, *5*, 252−255.
(24) Gite, V. V.; Kulkarni, R. D.; Hundiwale, D. G.; Kapadi, U. R. Synthesis and Characterisation of Polyurethane Coatings Based on Trimer of Isophorone Diisocyanate (IPDI) and Monoglycerides of Oils. *Surf. Coat. Int., Part B* **2006**, *89*, 117−122.
(25) Nejati, E.; Mirzadeh, H.; Zandi, M. Synthesis and Characterization of Nano-Hydroxyapatite Rods/Poly(L-lactide acid) Composite Scaffolds for Bone Tissue Engineering. *Composites, Part A* **2008**, *39*, 1589−1596.
(26) Princi, E.; Vicini, S.; Stagnaro, P.; Conzatti, L. The Nanostructured Morphology of Linear Polyurethanes Observed by Transmission Electron Microscopy. *Micron* **2011**, *42*, 3−7.
(27) Liff, S. M.; Kumar, N.; McKinley, G. H. High-Performance Elastomeric Nanocomposites via Solvent-Exchange Processing. *Nat. Mater.* **2007**, *6*, 76−83.
(28) Salgado, A. J.; Coutinho, O. P.; Reis, R. L. Bone Tissue Engineering: State of the Art and Future Trends. *Macromol. Biosci.* **2004**, *4*, 743−765.
(29) Puppi, D.; Mota, C.; Gazzarri, M.; Dinucci, D.; Gloria, A.; Myrzabekova, M.; Ambrosio, L.; Chiellini, F. Additive Manufacturing of Wet-Spun Polymeric Scaffolds for Bone Tissue Engineering. *Biomed. Microdevices* **2012**, *14*, 1115−1127.
(30) Shuai, C.; Mao, Z.; Han, Z.; Peng, S.; Li, Z. Fabrication and Characterization of Calcium Silicate Scaffolds for Tissue Engineering. *J. Mech. Med. Biol.* **2014**, *14*, 1450049.
(31) Shirazi, S. F. S.; Gharehkhani, S.; Mehrali, M.; Yarmand, H.; Metselaar, H. S. C.; Adib Kadri, N.; Osman, N. A. A. A Review on Powder-Based Additive Manufacturing for Tissue Engineering: Selective Laser Sintering and Inkjet 3D Printing. *Sci. Technol. Adv. Mater.* **2015**, *16*, 033502.
(32) Espinosa, H. D.; Rim, J. E.; Barthelat, F.; Buehler, M. J. Merger of Structure and Material in Nacre and Bone−Perspectives on de novo Biomimetic Materials. *Prog. Mater. Sci.* **2009**, *54*, 1059−1100.
(33) Amoroso, N. J.; D'Amore, A.; Hong, Y.; Wagner, W. R.; Sacks, M. S. Elastomeric Electrospun Polyurethane Scaffolds: the Interrelationship between Fabrication Conditions, Fiber Topology, and Mechanical Properties. *Adv. Mater.* **2011**, *23*, 106−111.
(34) Xiang, C.; Cox, P. J.; Kukovecz, A.; Genorio, B.; Hashim, D. P.; Yan, Z.; Peng, Z.; Hwang, C. C.; Ruan, G.; Samuel, E. G.; Sudeep, P. M.; Konya, Z.; Vajtai, R.; Ajayan, P. M.; Tour, J. M. Functionalized Low Defect Graphene Nanoribbons and Polyurethane Composite Film for Improved Gas Barrier and Mechancial Performances. *ACS Nano* **2013**, *7*, 10380−10386.
(35) Libonati, F.; Colombo, C.; Vergani, L. Design and Characterization of A Biomimetic Composite Inspired to Human Bone. *Fatigue Fract. Eng. Mater. Struct.* **2014**, *37*, 772−781.
(36) Finnigan, B.; Jack, K.; Campbell, K.; Halley, P.; Truss, R.; Casey, P.; Cookson, D.; King, S.; Martin, D. Segmented Polyurethane Nanocomposites: Impact of Controlled Particle Size Nanofillers on the Morphological Response to Uniaxial Deformation. *Macromolecules* **2005**, *38*, 7386−7396.
(37) Yeh, F.; Hsiao, B. S.; Sauer, B. B.; Michel, S.; Siesler, H. W. In-situ Studies of Structure Development During Deformation of A Segmented Poly(urethane-urea) Elastomer. *Macromolecules* **2003**, *36*, 1940−1954.
(38) Huang, L.; Yi, N.; Wu, Y.; Zhang, Y.; Zhang, Q.; Huang, Y.; Ma, Y.; Chen, Y. Multichannel and Repeatable Self-Healing of Mechanical Enhanced Graphene-Thermoplastic Polyurethane Composites. *Adv. Mater.* **2013**, *25*, 2224−2228.
(39) Khan, A. S.; Wong, F. S. L.; McKay, I. J.; Whiley, R. A.; Rehman, I. U. Structural, Mechanical, and Biocompatibility Analyses of A Novel Dental Restorative Nanocomposite. *J. Appl. Polym. Sci.* **2013**, *127*, 439−447.
(40) Ozcelik, B.; Blencowe, A.; Palmer, J.; Ladewig, K.; Stevens, G. W.; Abberton, K. M.; Morrison, W. A.; Qiao, G. G. Highly Porous and Mechanically Robust Polyester Poly(ethylene glycol) Sponges as Implantable Scaffolds. *Acta Biomater.* **2014**, *10*, 2769−2780.
(41) Thein-Han, W. W.; Misra, R. D. Biomimetic Chitosan-Nanohydroxyapatite Composite Scaffolds for Bone Tissue Engineering. *Acta Biomater.* **2009**, *5*, 1182−1197.
(42) Sun, H.; Zhu, F.; Hu, Q.; Krebsbach, P. H. Controlling Stem Cell-Mediated Bone Regeneration through Tailored Mechanical Properties of Collagen Scaffolds. *Biomaterials* **2014**, *35*, 1176−1184.

DOI: 10.1021/acsami.5b07327
ACS Appl. Mater. Interfaces 2015, 7, 22618−22629